Science Advances
AAAS

advances.sciencemag.org/cgi/content/full/5/2/eaau7728/DC1

Supplementary Materials for

Lithiophilicity chemistry of heteroatom-doped carbon to guide uniform lithium nucleation in lithium metal anodes

Xiang Chen, Xiao-Ru Chen, Ting-Zheng Hou, Bo-Quan Li, Xin-Bing Cheng, Rui Zhang, Qiang Zhang*

*Corresponding author. Email: zhang-qiang@mails.tsinghua.edu.cn

Published 15 February 2019, *Sci. Adv.* **5**, eaau7728 (2019)
DOI: 10.1126/sciadv.aau7728

This PDF file includes:

Supplementary Materials

1. Supplementary Figures

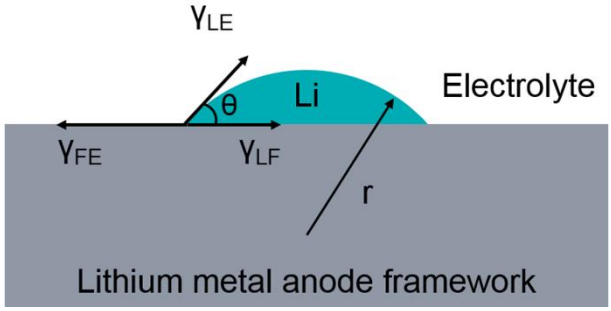

Fig. S1. Schematic representation of the Li nucleation on conductive frameworks based on the classical heterogeneous nucleation model.

According to classical heterogeneous nucleation theory, the critical nucleation radius (r^*) is determined by

$$r^* = 2\gamma_{LE} / \Delta G_V \quad \text{(S1)}$$

where ΔG_V is the free energy change of lithium from electrolyte to anode and γ_{LE} is lithium/electrolyte interfacial free energy. The critical nucleation radius (r^*) is unaffected by the anode framework. However, the volume of nucleated lithium to reach r^* is much smaller than that in homogeneous nucleation, indicating the important role of anode framework in regulating Li nucleation.

More importantly, the anode framework can regulate the heterogeneous nucleation barrier

$$\Delta G^*_{het} = S(\theta)\Delta G^*_{hom} \quad \text{(S2)}$$

$$S(\theta) = (2 + \cos\theta)(1 - \cos\theta)^2 / 4 \quad \text{(S3)}$$

where ΔG^*_{het} and ΔG^*_{hom} are the heterogeneous and homogeneous nucleation barrier, respectively.

Considering the balance in the plane of the framework

$$\cos\theta = (\gamma_{FE} - \gamma_{LF}) / \gamma_{LE} \quad \text{(S4)}$$

When the binding energy between lithium and framework is increased, γ_{LF} is reduced. Therefore, $\cos\theta$ is increased and $S(\theta)$ as well as ΔG^*_{het} is decreased.

In summary, a framework that can provide a large binding energy toward lithium can reduce the Li nucleation barrier as well as the volume of nucleated Li to reach r^*, favoring uniform Li deposition. The binding energy is thus a reasonable descriptor of the lithiophilicity of anode framework.

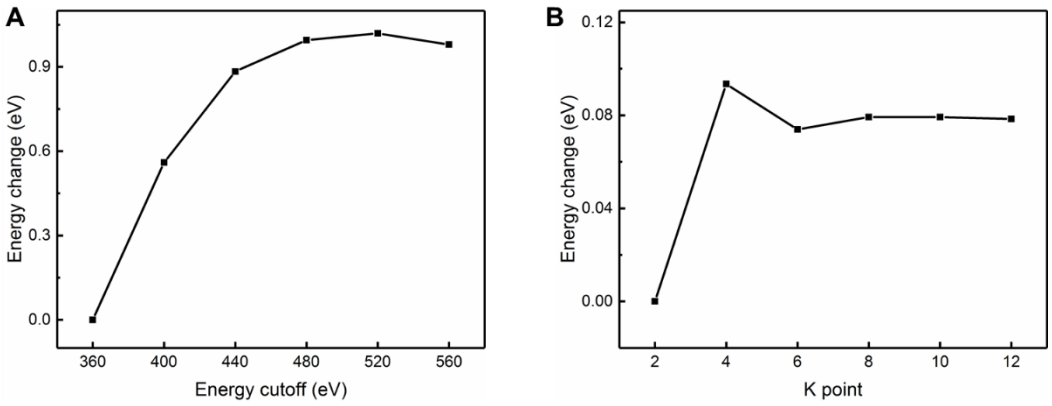

Fig. S2. Periodic calculation method test. (**A**) Energy cutoff and (**B**) K point.

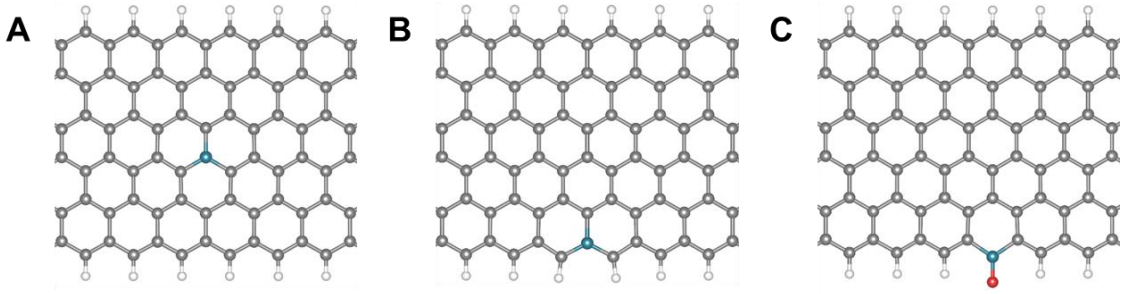

Fig. S3. The optimized configuration of carbons with bgB, egB, and oB dopant. The optimized configuration of carbons with (**A**) bgB, (**B**) egB, and (**C**) oB doping, respectively. The hydrogen, boron, carbon, and oxygen atoms are marked as white, green, gray, and red, respectively.

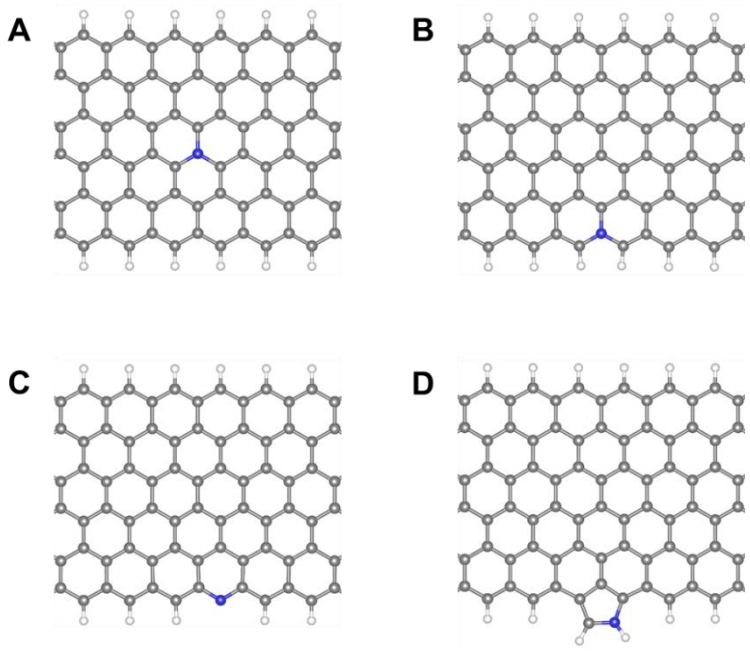

Fig. S4. The optimized configuration of carbons with bqN, eqN, pN, and rN dopant. The optimized configuration of carbons with (**A**) bqN, (**B**) eqN, (**C**) pN, and (**D**) rN doping, respectively. The hydrogen, nitrogen, and carbon atoms are marked as white, gray, and blue, respectively.

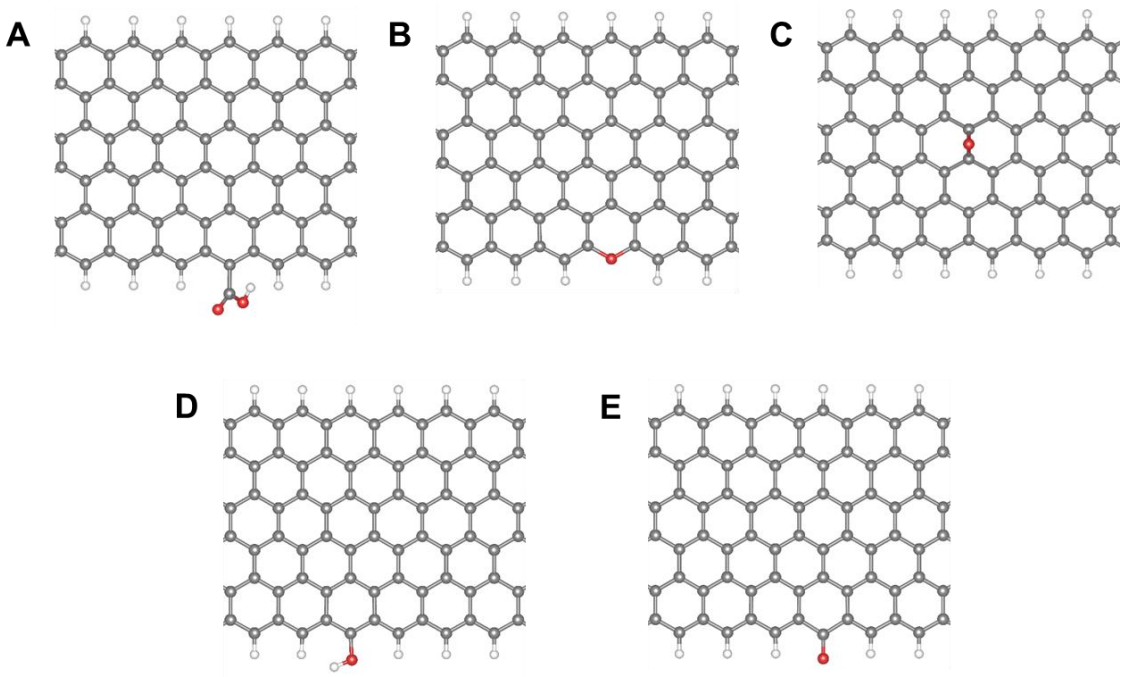

Fig. S5. The optimized configuration of carbons with aO, cO, eO, hO, and kO dopant. The optimized configuration of carbons with (**A**) aO, (**B**) cO, (**C**) eO, (**D**) hO, and (**E**) kO functional, respectively. The hydrogen, carbon, and oxygen atoms are marked as white, gray, and red, respectively.

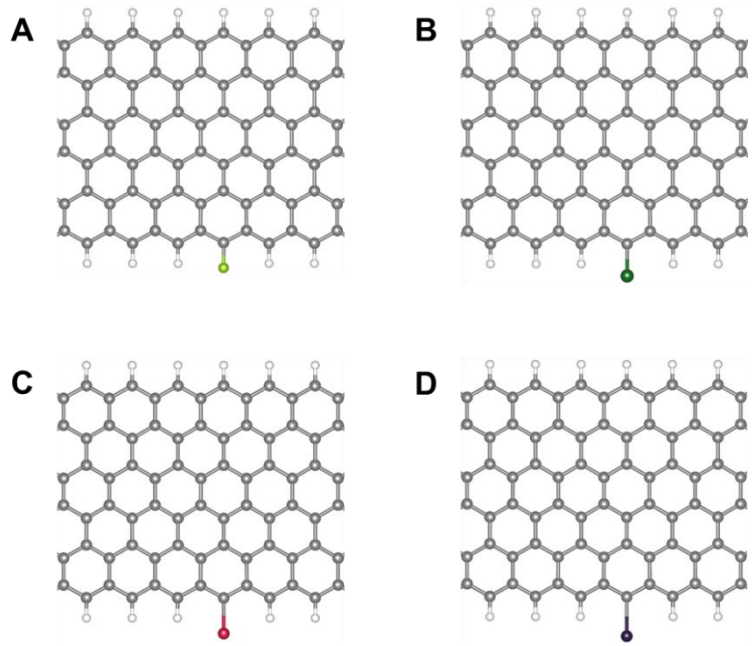

Fig. S6. The optimized configuration of carbons with F, Cl, Br, and I dopant. The optimized configuration of carbons with (**A**) F, (**B**) Cl, (**C**) Br, and (**D**) I doping, respectively. The hydrogen, carbon, fluorine, chlorine, bromine, and iodine atoms are marked as white, gray, cyan, bottle green, orange, and black, respectively.

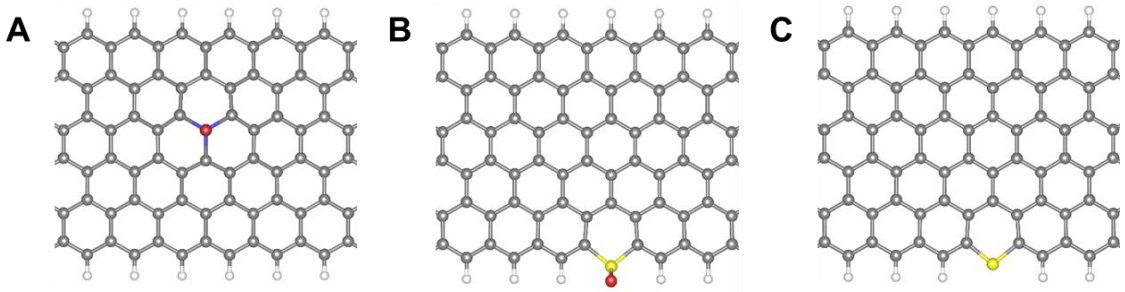

Fig. S7. The optimized configuration of carbons with P, oS, and S dopant. The optimized configuration of carbons with (**A**) P, (**B**) oS, and (**C**) S doping, respectively. The hydrogen, carbon, oxygen, phosphorus, and sulfur atoms are marked with white, gray, red, wathet, and yellow, respectively.

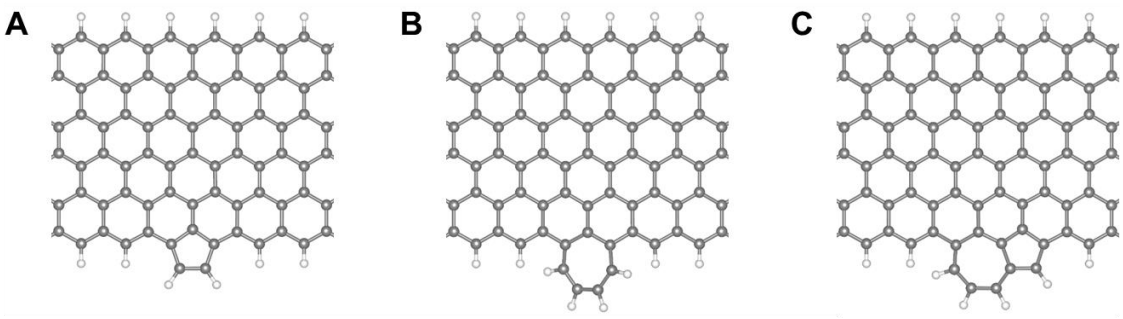

Fig. S8. The optimized configuration of carbons with C5, C7, and C5+C7 defects. The optimized configuration of carbons with (**A**) C5, (**B**) C7, and (**C**) C5+C7 defects, respectively. The hydrogen and carbon atoms are marked with white and gray, respectively

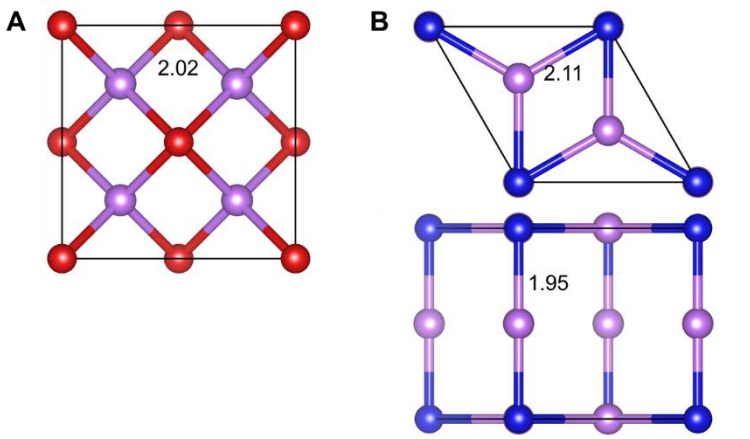

Fig. S9. The optimized crystal structures of Li_2O and Li_3N. The optimized crystal structures of (**A**) Li_2O and (**B**) Li_3N (top: top view; bottom: side view). The Li–O/N bond length is marked with black numbers. The lithium, nitrogen, and oxygen atoms are marked with purple, blue, and red, respectively.

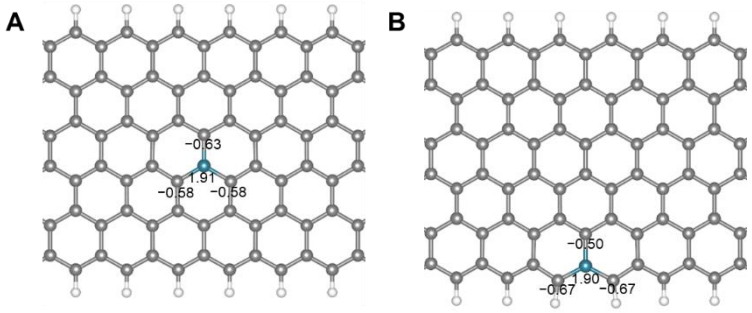

Fig. S10. The Bader charge analyses of bgB- and egB-GNRs. The Bader charge (marked with black numbers) analyses of (**A**) bgB and (**B**) egB. The hydrogen, boron, and carbon atoms are marked as white, green, and gray, respectively.

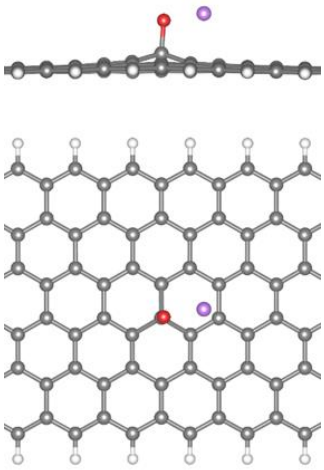

Fig. S11. The optimized interaction geometry of a Li atom interacts with eO-GNR. Top: side view; Bottom: top view. The pristine C–O–C bond was destroyed by the adsorbed Li atom. The hydrogen, lithium, carbon, and oxygen atoms are marked as white, purple, gray, and red, respectively.

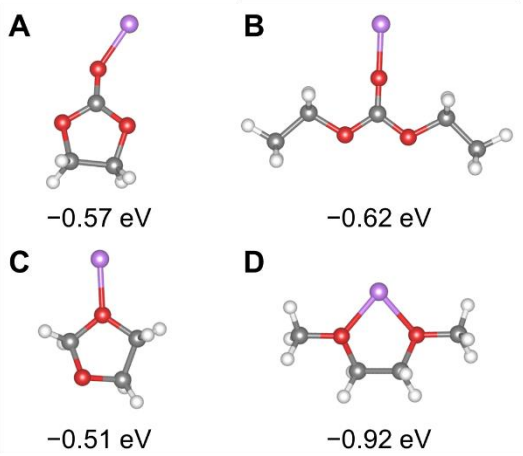

Fig. S12. The optimized structures and binding energies between a Li atom and a solvent molecule. (**A**) EC, (**B**) DEC, (**C**) DOL, and (**D**) DME.

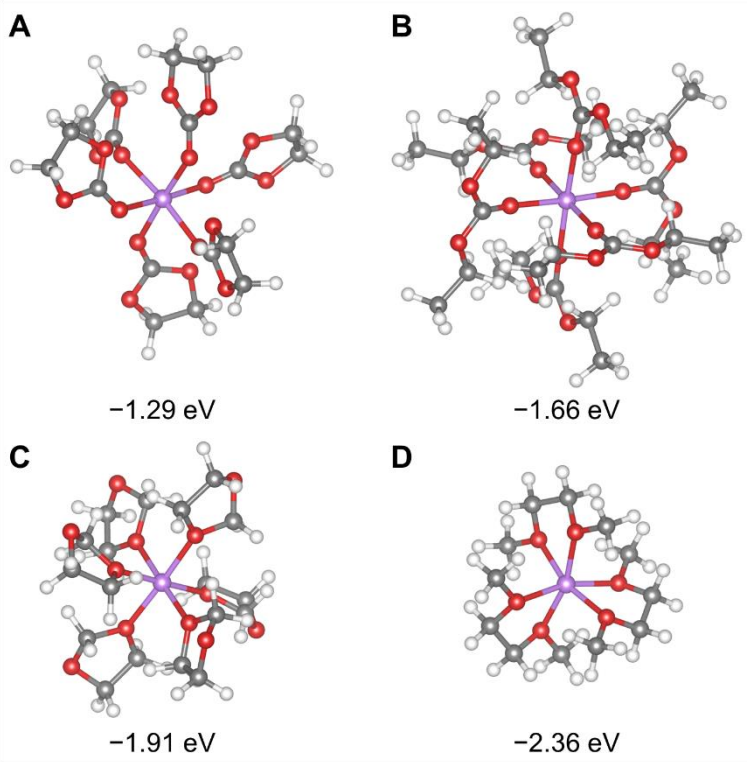

Fig. S13. The optimized structures and binding energies between a Li atom and a multisolvent molecule. (**A**) EC, (**B**) DEC, (**C**) DOL, and (**D**) DME.

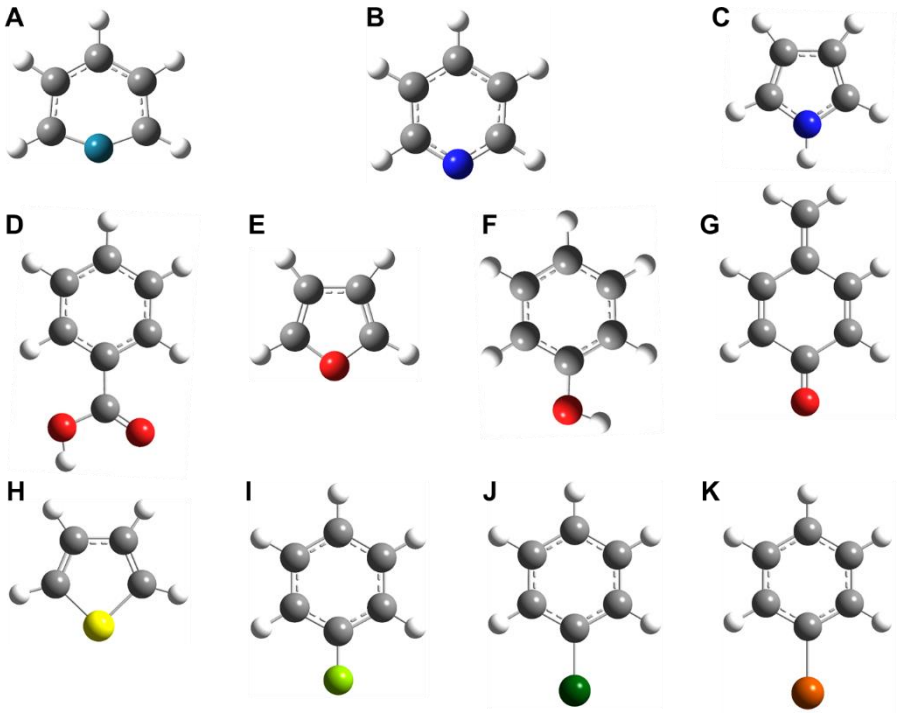

Fig. S14. The optimized structures of borabenzene, pyridine, pyrrole, benzoic acid, furan, phenol, quinomethan, thiophene, fluorobenzene, chlorobenzene, and bromobenzene molecules. The optimized structures of (**A**) borabenzene, (**B**) pyridine, (**C**) pyrrole, (**D**) benzoic acid, (**E**) furan, (**F**) phenol, (**G**) quinomethan, (**H**) thiophene, (**I**) fluorobenzene, (**J**) chlorobenzene, and (**K**) bromobenzene molecules. The hydrogen, boron, carbon, nitrogen, oxygen, fluorine, sulfur, chlorine, and bromine atoms are marked as white, green, gray, blue, red, cyan, yellow, bottle green, and orange, respectively.

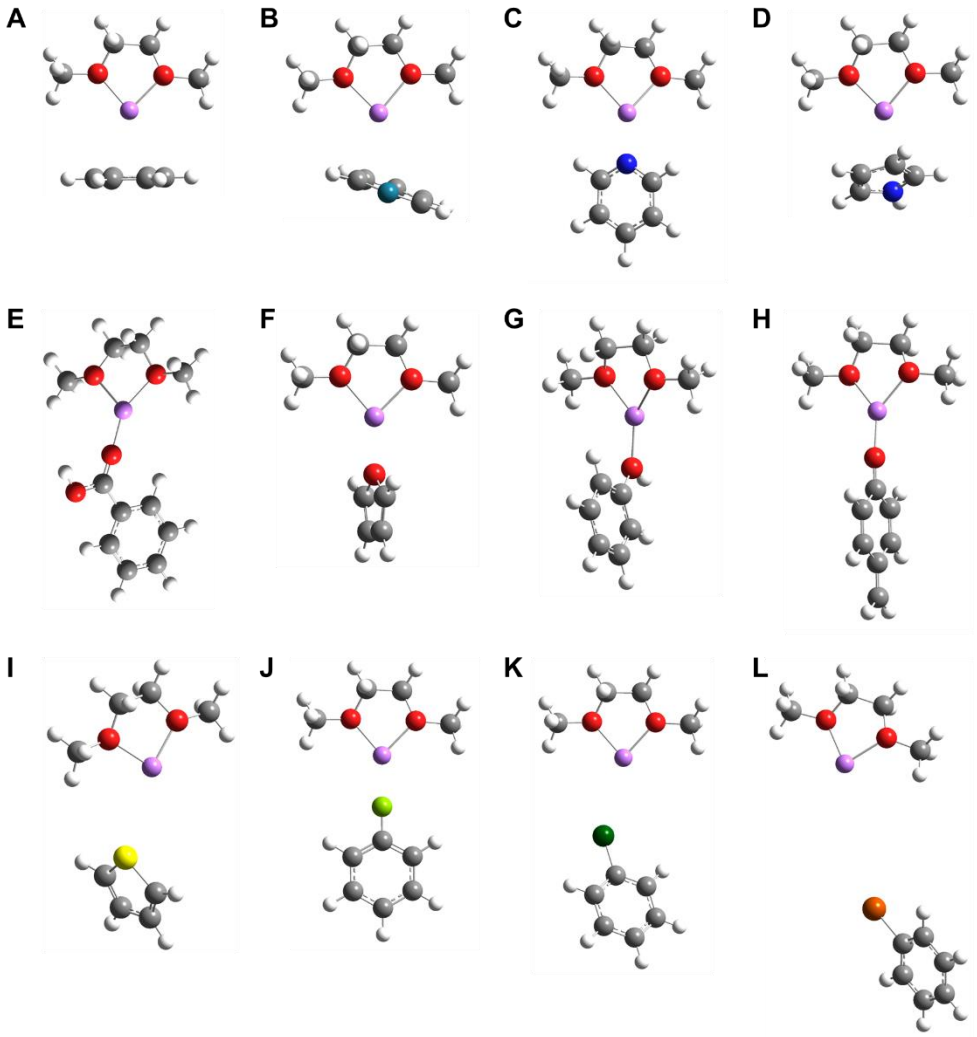

Fig. S15. The optimized interaction geometries of Li^+–DME complex and borabenzene, pyridine, pyrrole, benzoic acid, furan, phenol, quinomethan, thiophene, fluorobenzene, chlorobenzene, and bromobenzene molecules. The optimized interaction geometries of Li^+–DME complex and (**A**) benzene, (**B**) borabenzene, (**C**) pyridine, (**D**) pyrrole, (**E**) benzoic acid, (**F**) furan, (**G**) phenol, (**H**) quinomethan, (**I**) thiophene, (**J**) fluorobenzene, (**K**) chlorobenzene, and (**L**) bromobenzene molecules. The hydrogen, lithium, boron, carbon, nitrogen, oxygen, fluorine, sulfur, chlorine, and bromine atoms are marked as white, purple, green, gray, blue, red, cyan, yellow, bottle green, and orange, respectively.

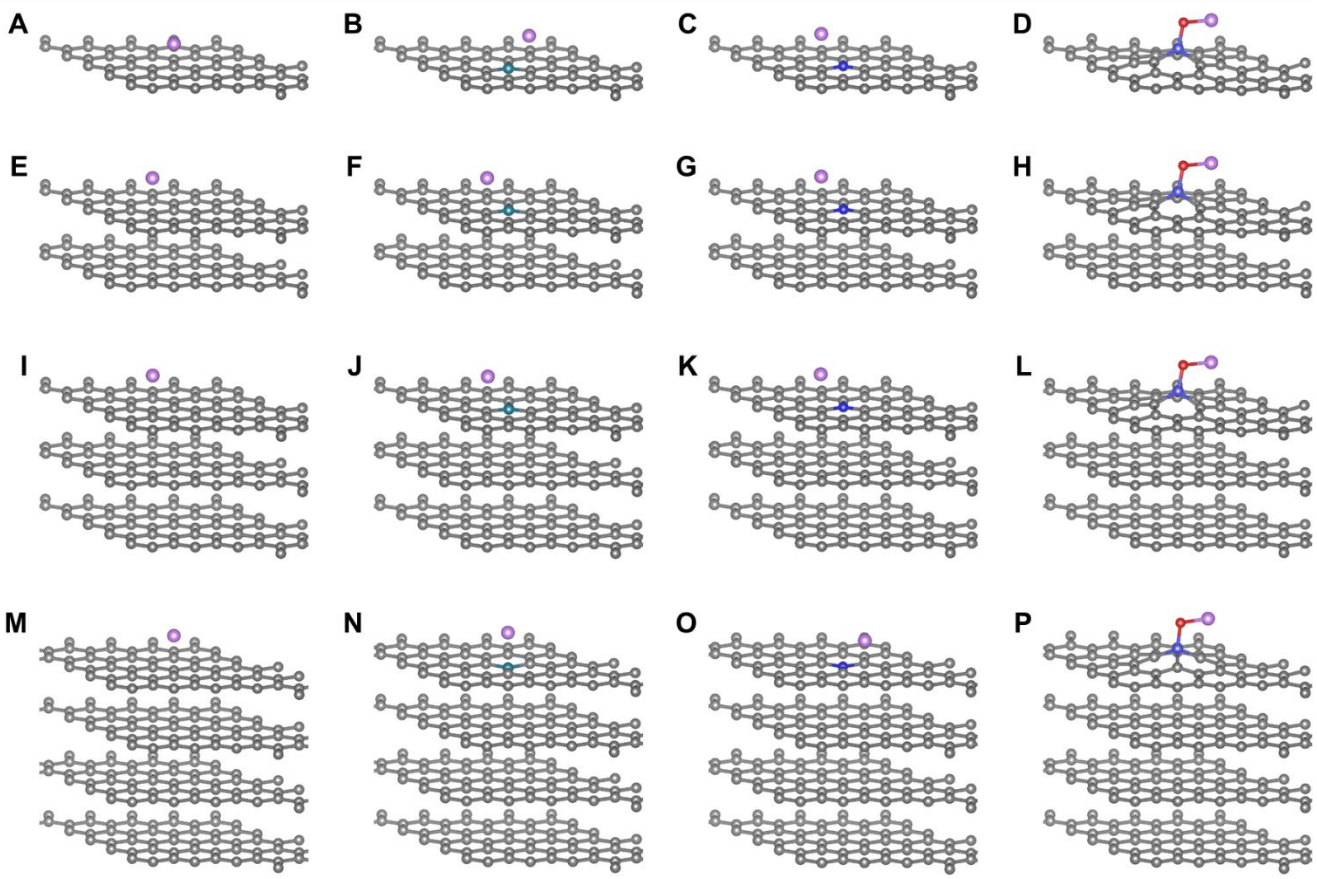

Fig. S16. The optimized interaction geometry of a Li atom and single-/multilayered graphene and graphite. (**A**) Single-layered graphene and single-layered graphene with (**B**) bgB, (**C**) bqN, and (**D**) P dopant. (**E**) Bi-layered graphene and bi-layered graphene with (**F**) bgB, (**G**) bqN, and (**H**) P dopant. (**I**) Triple-layered graphene and triple-layered graphene with (**J**) bgB, (**K**) bqN, and (**L**) P dopant. (**M**) Graphite and graphite with (**N**) bgB, (**O**) bqN, and (**P**) P dopant. The hydrogen, lithium, boron, carbon, nitrogen, oxygen, and phosphorus atoms are marked as white, purple, green, gray, blue, red, and wathet, respectively.

Herein, 2D periodic graphene models rather than GNR models were used to investigate the effects of the number of graphene layer as multi-layered GNR models are very complicated. The binding energy of lithium on 2D single-layered graphene (–1.15 eV) is smaller than that on pure GNR (–1.91 eV) due to edge effects. The bgB and bqN decorations were selected as representatives of single doping that enhances and weakens the interaction between graphene and lithium, respectively. Besides, P/O co-doping is selected as the representative of co-doping models.

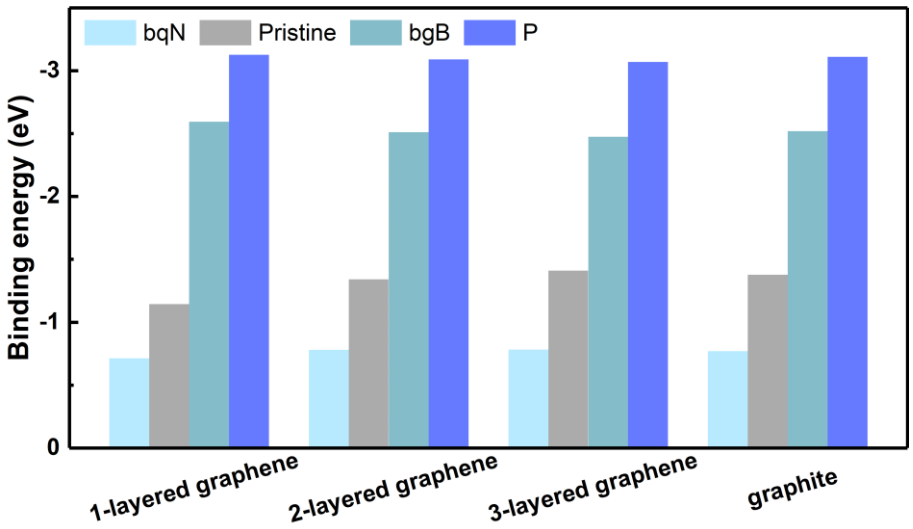

Fig. S17. A summary of calculated binding energy between a Li atom and single/multilayered graphene and graphite.

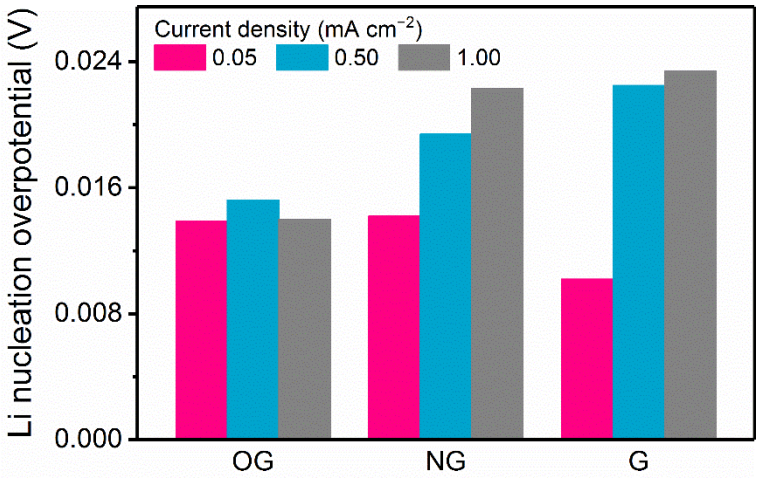

Fig. S18. The Li nucleation overpotentials on G, NG, and OG electrodes at different current densities (0.05, 0.50, and 1.00 mA cm^{-2}).

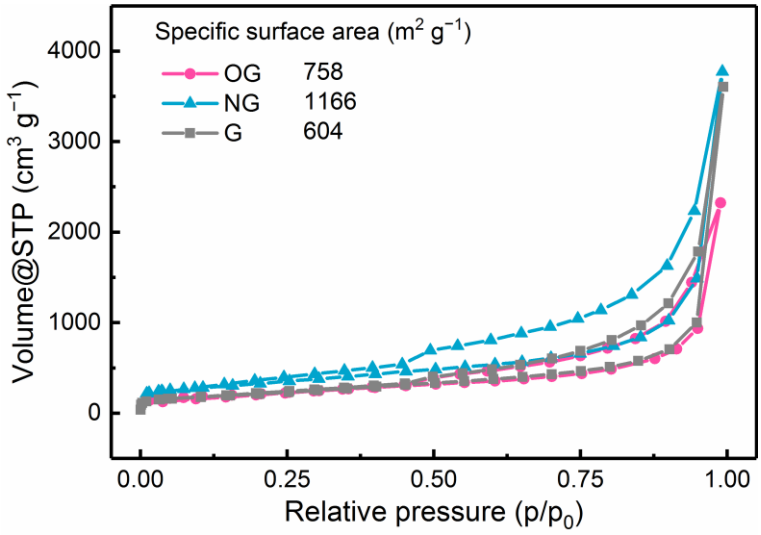

Fig. S19. The N_2 isotherms of OG, NG, and G materials.

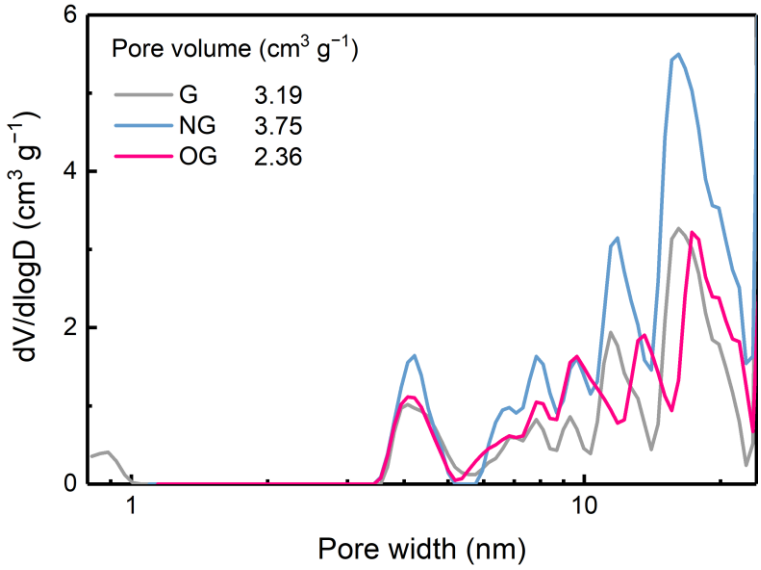

Fig. S20. The pore size distribution derived from the N_2 isothermal adsorption plot of OG, NG, and G materials.

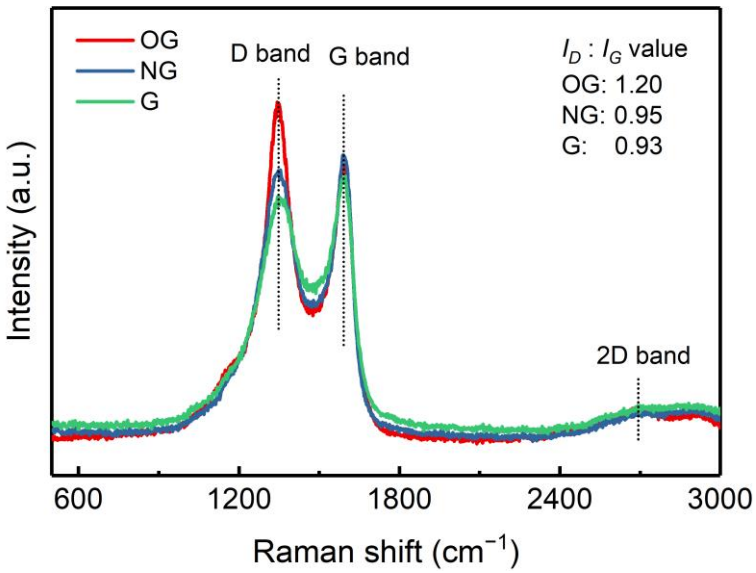

Fig. S21. The Raman spectra of OG, NG, and G materials.

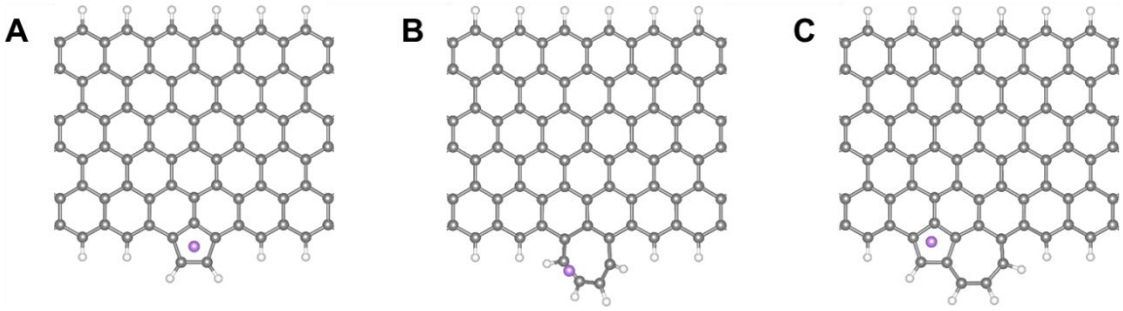

Fig. S22. The optimized interaction geometry of Li atom on GNR with C5, C7, and C5+C7 defects. The optimized interaction geometry of Li atom on GNR with (**A**) C5, (**B**) C7, and (**C**) C5+C7 defects, respectively. The hydrogen, lithium, and carbon atoms are marked as white, purple, and gray, respectively.

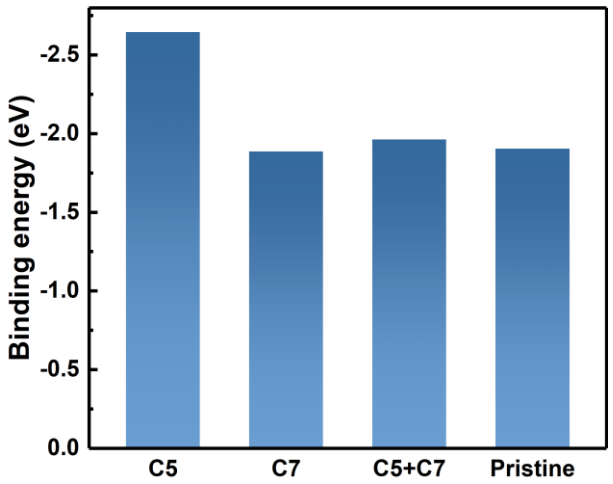

Fig. S23. The summary of binding energy of a Li atom adsorbed on GNR with C5, C7, and C5 + C7 defects.

2. Supplementary Tables

Table S1. A summary of binding energy between nanoribbons and a Li atom.

Type of GNR	Binding energy (eV)
egB	−2.54
bgB	−2.59
oB	−3.59
bqN	−1.17
eqN	−1.30
rN	−1.39
pN	−2.40
cO	−1.04
eO	−1.64
hO	−1.91
kO	−2.35
aO	−2.86
F	−0.83
Cl	−0.48
Br	−0.45
I	−0.84
P	−3.14
S	−0.57
oS	−2.60
pristine	−1.91

Table S2. A summary of Li binding energy on Li (100) and (110) surfaces and total energy per bulk lithium.

Energy (eV)	Li (100)	Li (110)	Bulk lithium
	−1.33	−1.41	−1.90

Table S3. A summary of local dipole in heteroatom-doped nanoribbons.

Type of GNR	Local dipole (e^{-} Å)
egB	1.90
bgB	1.66
oB	3.21
bqN	0.60
eqN	0.66
rN	0.57
pN	0.64
cO	0.63
hO	0.85
kO	1.11
aO	2.00
F	0.38